Published in final edited form as:

FASEB J. 2020 January ; 34(1): 912–929. doi:10.1096/fj.201902359R.

Membrane-type frizzled-related protein regulates lipidome and transcription for photoreceptor function

Marie-Audrey I. Kautzmann[*], **William C. Gordon**[*], **Bokkyoo Jun**[*], **Khanh V. Do**[*], **Blake J. Matherne**[*,1], **Zhide Fang**[†], **Nicolas G. Bazan**[*,2]

[*]Neuroscience Center of Excellence, School of Medicine, Louisiana State University Health New Orleans, New Orleans, Louisiana, USA;

[†]Biostatistics, School of Public Health, Louisiana State University Health Sciences Center, New Orleans, Louisiana, USA.

Abstract

Molecular decision-makers of photoreceptor (PRC) membrane organization and gene regulation are critical to understanding sight and retinal degenerations that lead to blindness. Using *Mfrp*^{rd6} mice, which develop PRC degeneration, we uncovered that Membrane-type Frizzled-Related Protein (MFRP) participates in docosahexaenoic acid (DHA, 22:6) enrichment in a manner similar to Adiponectin Receptor 1 (AdipoR1). Untargeted imaging mass spectrometry demonstrates cell-specific reduction of phospholipids containing 22:6 and very-long-chain polyunsaturated fatty acids (VLC-PUFAs) in *Adipor1*$^{-/-}$ and *Mfrp*^{rd6} retinas. Gene expression of pro-inflammatory signaling pathways are increased and gene-encoding proteins for PRC function decrease in both mutants. Thus, we propose that both proteins are necessary for retinal lipidome membrane organization, visual function and to the understanding of the early pathology of retinal degenerative diseases.

Keywords

retinal degenerations; VLC-PUFAs; Adipor1; Matrix-assisted laser desorption/ionization imaging mass spectrometry (MALDI IMS); RPE cell; inflammatory signaling

1. Introduction

MFRP is a glycosylated transmembrane protein with an extracellular frizzled-related cysteine-rich domain (1, 2) that recognizes frizzled Wnt receptors (2, 3), and participates in cell fate and development (1, 3). *MFRP* is expressed in the retinal pigment epithelium (RPE) and ciliary bodies (2), and gene mutations encoding this protein are associated with

[2]Correspondence: Nicolas G. Bazan, Neuroscience Center of Excellence, School of Medicine, Louisiana State University Health Sciences Center, 2020 Gravier Street, Suite D, New Orleans, LA 70112, USA. nbazan@lsuhsc.edu.

[6]·Author Contributions

N.G.B. conceived the study; B.J. conducted the lipidomic analysis (LC-MS/MS and MALDI); histology was performed by W.C.G.; M.A.K. and K.D. performed the gene analysis; M.A.K. conducted the OCT analysis; B.M. acquired the fundus images and performed ERG; N.G.B., B.J., M.A.K. and W.C.G. designed experiments and analyzed the data; Z.F, performed the statistical analysis; W.C.G., M.A.K. and N.G.B wrote the paper with input from all other authors. All authors have read and approved the manuscript.

[1]Current affiliation: University of Mississippi Medical Center, Jackson, Mississippi, USA.

photoreceptor cell (PRC) degeneration, nanophthalmos, posterior microphthalmia, retinitis pigmentosa, foveoschisis, and optic disc drusen (4). The *rd6* mice displays a mutated MFRP and also leads to retinal degeneration (2). Fundus analysis of these mice reveals discrete dots across the retina due to macrophage infiltration in the subretinal space (5–7) as in flecked retinal diseases (8) with similarities to human *retinitis punctata albescens* (7, 9). *Mfrp*^{rd6} has a 4 bp deletion in a splice donor sequence resulting in exon 4 being skipped, and in a truncated protein (2).

Although *MFRP* mutations are linked to PRC degeneration, there is an incomplete understanding of MFRP protein function (10, 11) and its potential association with ADIPOR1 (*Adipor1*) including a shared pathogenic mechanism due to phenotypic similarities of the mutants of these two proteins (10). Moreover, comparisons of *Mfrp*^{rd6} mice with wild-type (WT) littermates revealed the absence of ADIPOR1 in the RPE (10), but retention in the retina, which suggested that an ADIPOR1 deficiency in RPE may initiate retinal degeneration in *rd6* mice (10).

ADIPOR1 is expressed in the retina and RPE, and the mutant of the *Adipor1* gene in these cells results in inability to take up and incorporate docosahexaenoic acid (DHA, 22:6,n-3), loss of PRC, and retinal degeneration (10, 12). A single amino acid mutation of *Adipor1* occurs in different forms of retinitis pigmentosa (13, 14). Polymorphisms of this receptor have been found in age-related macular degeneration (AMD) (15) as well as in other forms of retinal degenerations. 22:6 is an omega-3 (n-3) essential fatty acid highly enriched in and required for the biogenesis of PRC membranes (16) and is supplied either directly by diet or synthesized from dietary linolenic acid in the liver (18:3,n-3) (17). 22:6 supplied by the liver (18) is taken up from the choriocapillaris by the RPE and then delivered to the PRC inner segments (16, 19). Here, it is incorporated at the sn-2 position of the glycerol backbone, especially in phosphatidylcholine (PC), which comprises more than 50% of PRC phospholipids (20) mainly used for the biogenesis of PRC outer segments (21, 22). 22:6-containing phospholipids modulate lipid rafts (23), become associated with RHODOPSIN (24), and permit efficient conformational changes of RHODOPSIN and its associated G proteins as photons are absorbed (25–27). The inability of the retina to take up and incorporate 22:6 leads to homeostatic compromise and PRC death as in retinal degenerative diseases (12, 22, 28). PRC outer segment tips containing 22:6-rich disks are phagocytized daily by the RPE, and the 22:6 is recycled back to PRC (16, 19). PRC also contain very long-chain polyunsaturated fatty acids (VLC-PUFAs; ≥ 28 carbons) formed by ELOVL4 (ELOngation of Very Long chain fatty acids-4) (29, 30) that elongate 26:6,n-3 derived from 22:6 or 22:5,n-3 (eicosapentaenoic acid, EPA) (31, 32). Despite the low abundance of retinal 22:5 compared to 22:6, 22:5 is the favored substrate for VLC-PUFA production (32). Generated by retro-conversion from 22:6 in peroxisomes, 22:5 provides the 22:6 substrate for ELOVL4 (32). ELOVL4 synthesizes VLC-PUFAs in retina (21, 33) and testes (34), and generates VLC-saturated fatty acids (VLC-SFAs) in skin and brain (35, 36). VLC-PUFAs in PRC then become acyl chains of PC, incorporating at the sn-1 position (37). Under uncompensated oxidative stress (UOS), 32C and 34C VLC-PUFAs are released and converted to elovanoids (ELVs) through enzymatic lipoxygenation as a PRC protective response (37). Because UOS also triggers 22:6 release and conversion to neuroprotectin D1

(NPD1) (28), 22:6 availability is part of a dual protective signaling which sustains PRC integrity (28).

To maintain fundamental PRC functions, membrane phospholipids provide an environment for phototransduction to proceed, and precursors of biologically active lipid mediators in the inner segment of PRC, as well as in the RPE (28, 37). Therefore, a tight balance on retinal lipidome homeostasis must be maintained because UOS affects highly unsaturated fatty acids, forming 22:6 protein adducts that contribute to retinal degeneration (38). Overall, a healthy retinal lipidome is essential for PRC function within a highly stressful environment of bright light, high-oxygen demands, and an abundance of polyunsaturated fatty acids which are highly susceptible to oxidative damage (19, 28).

Here, utilizing the *Mfrp*^{rd6} mouse, we have characterized key events that lead to PRC degeneration by mass spectrometry imaging, LC-MS/MS, physiology, and transcriptomic approaches. We have shown phenotypical, histological, and physiological similarities between *Adipor1*$^{-/-}$ and *Mfrp*^{rd6} mouse retinas with comparable onset of PRC degeneration. Retinas and RPE in both mice presented a dramatic and selective deficit of 22:6,n-3-containing PC phospholipids, but not of arachidonic acid (20:4,n-6)-containing molecules, and an absence of VLC-PUFAs in the retina. We compared gene expression profiles of *Adipor1*$^{-/-}$ and *Mfrp*^{rd6} mice and found *Casp1* and *Pycard*, part of the pyroptotic cell death pathway, upregulated in both mutants. Further analysis of target genes in enriched pathways indicated that the mutation of ADIPOR1 in the retina resulted in upregulation of genes belonging to JNK phosphorylation and activation mediated by the activated human TAK1 pathway, while the mutation of MFRP was linked to activation of the NOD-like receptor signaling pathway. Overall, our results indicate that the inability to enrich the retina with 22:6 results in the absence of VLC-PUFAs from the lipidomes of *Adipor1*$^{-/-}$ and *Mfrp*^{rd6} mice, and, consequently, the inability to synthesize the neuroprotective elovanoids, which correlates with the activation of inflammatory signaling pathways and the onset of retinal degeneration.

2. Materials and methods

2.1. Animals

Throughout this study C57BL6/J (wild type; WT, The Jackson Laboratory, stock # 000664), B6.129P2-Adipor1tm1Dgen/Mmnc (*Adipor1*$^{-/-}$; MMRRC, stock # 011599-UNC) and B6.C3Ga-*Mfrp*^{rd6}/J (*Mfrp*^{rd6}; The Jackson Laboratory, stock # 003684) male and female mice were used. Mice were maintained in the LSU animal colony on a 12 h:12 h light cycle at ~30 lux (light on-set was at 0600 h), and given water and food *ad libitum*. *Adipor1*$^{-/-}$ and *Mfrp*^{rd6} were screened for *Crb1* (*rd8*) mutation by PCR according to (51), and we confirmed that they do not contain an inherent *Crb1* mutation, hence, the retinal phenotypes observed in these mice derive from the mutations of *Adipor1* and *Mfrp*. Summary of the Mouse Universal Genotyping Array (MUGA) and MMRRC computational tools used to assess the genetic background of the *Adipor1*$^{-/-}$ mice can be found at: http://www.csbio.unc.edu/MMRRC/index.py?run=StatsTable.viewSample&sample=3826&mm=0. All experiments were conducted in accordance with the Association for Research of Vision and Ophthalmology (ARVO) statement for the use of animals in ophthalmic and vision research,

and the protocols were approved by the Institutional Animal Care and Use Committee (IACUC) for the LSU Health Sciences Center.

2.2. Spectral Domain-Optical Coherence Tomography (SD-OCT)

Fundus images of 3-month-old and SD-OCT images of WT, *Adipor1*$^{-/-}$, and *Mfrp*^{rd6} retinas of 1, 3, and 5 months of age were obtained (Heidelberg Spectralis HRA OCT system; Heidelberg Engineering, Heidelberg, Germany) as previously described (12), and viewed with ImageJ (http//imagej.nih.gov/ij). The thickness of the outer retina (PRC + RPE) was defined as the distance from the proximal edge of the outer plexiform layer nuclear layer to the tips of the photoreceptor outer segments; the inner retina thickness was defined as the distance from the distal edge of the inner nuclear layer to the proximal edge of the ganglion cell/nerve fiber layer (52). Three animals/genotype/time point were analyzed.

2.3. Electroretinograms

Conventional electroretinograms (ERGs) techniques were employed to determine general health and to follow physiological changes within the retinas of the experimental animals. Animals were dark adapted overnight (12–16 hours), anesthetized, and pupils dilated with topical 1.0% atropine (Mydriacyl 1%, Alcon). Body temperature was maintained at 38°C throughout by the recording platform of the Espion ERG apparatus (Diagnosys, Lowell, MA). A drop of 1% methylcellulose placed on the cornea prevented corneal desiccation and provided improved electrical contact. Fiber optics contacted the corneas and delivered the light flashes generated by the Espion system. Scotopic ERG responses were elicited with short duration LED flashes delivered from the Espion ERG apparatus, with interstimulus intervals of 0.5–2 min, depending on intensity. Flash intensities ranged from 0.0001–10 cd-s/m^2. Three–four responses were averaged for each step, depending on the stimulus intensity (the flash interval was adjusted to assure dark adaptation following the previous flash). ERG responses were filtered (low-pass 0.125 Hz, high-pass 300 Hz) and archived for later analysis. Intensity-response amplitude data were displayed on log-linear coordinates.

2.4. Matrix-assisted laser desorption/ionization imaging mass spectrometry (MALDI IMS)

Whole eyes of 2-month-old mice were embedded in gelatin, frozen, cryosectioned (20 μm thickness), and then collected on alternating glass slides (for staining with hematoxylin and eosin) and coverslips (for MALDI IMS). Coverslips were attached to MALDI stainless steel plates using thermally conductive dual tape. Plates were then attached to a magnet (thermally conductive) glued to the bottom of a sublimation chamber. 2,5-dihydroxybenzoic acid (DHB) (Fisher Scientific, Pittsburg, PA) formed the matrix for the positive ion mode. A Synapt G2-Si (Waters, Milford, MA), equipped with a MALDI source that uses a solid-state laser (355 nm) at a firing rate of 2000 Hz for positive ion mode data collection, was employed. HDImaing software (Waters, Milford, MA) was used to design the pattern of tissue scanning (30 μm spatial resolution for both horizontal and vertical movement) and data analysis. Each image spot consisted of a collection of 1 s data acquisition. Ions created by the MALDI source were further separated by ion-mobility-separation with helium gas in the TriWave region of the instrument, with an ion-mobility-separation wave velocity of 600 m/s and height of 40.0 V. Data processed with HDImaging was converted with an in-house program, and BioMap software (Novartis) was used to generate images.

2.5. Phospholipids molecular species as regional markers

Prior to analysis, specific markers for retinal layers/cell types were determined. To ensure good separation of retina and RPE-eyecup data, anterior segments were removed and retinas and RPE-eyecups were isolated separately on nitrocellulose filters, frozen, cryosectioned, and analyzed by MALDI IMS. PRCs were highly enriched with m/z 756.6 PC(16:0/16:0), m/z 760.6 PC(16:0/18:1) labeled the inner retina, m/z 1046.8 PC(34:6/22:6) denoted an n-3 derived VLC-PUFA, and m/z 738 (not identified) demarked the uvea/RPE complex. The shorthand notation used for lipid species here follows those outlined by Liebisch (53). The PC lipids observed (positive ion mode) were identified to lipid species level by collision induced dissociation (CID) and are indicated by the number of acyl carbons (C) and the number of double bonds, for example PC(56:12). Lipids were identified to the fatty acyl level by CID and are indicated by the fatty acyl groups esterified to the sn-1 and sn-2 position, such as PC(34:6/22:6). To determine which phospholipids were most abundant between retinas, difference spectra were generated. Equal areas were selected from identical regions of retinal sections and total spectra obtained from 700–1100 m/z. One spectrum was then subtracted from a spectrum of another animal to produce a difference spectrum, which revealed molecular abundance within the two retinas. If the remaining peaks extended upward, there was more of that molecule within retina 1, while peaks extending downward indicated more within retina 2. Possible identification was then assigned to these PCs, and corresponding MALDI IMS retinal images obtained. WT and mutant retinas were compared in this manner. Since spectrum amplitudes differ among retinas, even if normalized, this method only revealed very large differences that were considered interesting; quantitation using this method is inaccurate.

2.6. Lipid Extraction and Mass Spectrometry for Analysis by XevoTQ-S

Lipid extraction was performed similarly to our previous work (12). Briefly, each sample was homogenized in MeOH (3ml) followed by addition of $CHCl_3$ (6ml) and the internal standard (PC 28:0). After sonication in a water bath, samples were centrifuged, and the supernatant was added with pH 3.5 H_2O for phase separation. The bottom phase (organic phase) was dried down under N_2 and re-constituted in an AcN:MeOH:$CHCl_3$ (90:5:5) solution. A Xevo TQ-S equipped with Acquity UPLC BEH HILIC 1.7 μm 2.1 × 100 mm column was used with solvent A (acetonitrile:water, 1:1; 10 mM ammonium acetate pH 8.3) and solvent B (acetonitrile:water, 95:5; 10 mM ammonium acetate pH 8.3) as the mobile phase. Solvent B (100%) ran for the first 5 minutes isocratically, was graduated to 20% solvent A for 8 minutes, and then ran at 65% of A for 0.5 minutes. It ran isocratically at 65% of A for 3 minutes, and then returned to 100% of B for 3.5 minutes for equilibration. The capillary voltage was 2.5 kV, desolvation temperature was set at 550°C, the desolvation gas flow rate was 800 L/h, cone gas was 150 L/h, and nebulizer pressure was 7.0 Bars with the source temperature at 120°C. Mutant and WT samples for males and females (n=3 each) were treated and analyzed separately. There was no difference observed between the two sexes, therefore, we combined the data for each type of mouse for n = 6.

2.7. LC-MS/MS data analysis

Raw mass spectrometry data was based on percent composition of relative molecular species per biological replicate. Determination of differentially occurring molecular species was carried out using the loading score for the top ten PC molecular species for principle component 1, Principal component analysis (PCA),[1] hierarchical clustering and visualization of significant overlapping PCs (Venn diagram). Visualization of selected 22:6-containing and 20:4-containing PCs was obtained using BioVinci software (v1.1.3, r20180606), © 2017 BioTuring Inc., San Diego, CA, USA.

2.8. RNA isolation and cDNA preparation

Retinas and RPE-eyecups from 1-month-old WT, *Adipor1*$^{-/-}$ and *Mfrp*^{rd6} animals (n=6 each) were isolated. Mutant and WT samples for males and females (n=3 each) were treated and analyzed separately. There was no difference observed between the two genders, therefore, we combined the data for each type of mouse for n = 6. Total RNA was extracted using RNeasy Plus Mini Kit (Qiagen, Germantown, MD) according to the manufacturer's instructions. One microgram of RNA was reverse transcribed using an iScript cDNA Synthesis Kit (Bio-Rad, Hercules, CA). Diluted cDNA (100 ng, 1.25 μl) was used for the preamplification reaction by adding 1 μl of PreAmp Master Mix (Fluidigm, San Francisco, CA), 0.5 μl of a mix of all primers, and water to a final volume of 5 μl. The temperature profile was 95°C for 2 min followed by 12 cycles of amplification (95°C for 15 s, and 60°C for 4 min using the Bio-Rad CFX96 thermocycler). Each preamplification reaction of cDNA was then subjected to Exonuclease I treatment, to remove unincorporated primers. The resulting preamplified and treated cDNA was then diluted 5 times in TE Buffer.

2.9. High Throughput qPCR

The qPCR reaction mixture had a volume of 5 μl and contained 2.25 μl of diluted preamplified cDNA, 0.25 μl of DNA Binding Dye (Fluidigm) and 2.5 μl SsoFast EvaGreen Supermix with low ROX (Bio-Rad). The primer reaction mixture had a final volume of 5 μl and contained 2.5 μl Assay Loading Reagent (Fluidigm) and 0.25 μl of a mix of all reverse and forward primers, corresponding to a final concentration of 500 nM in the reaction. The Biomark 96.96 IFC™ (Integrated Fluidic Circuit) was first primed with an oil solution in the Juno™ Controller (Fluidigm) to fill the fluidic circuit. 96 sample reactions (5 μl each) were loaded into individual sample wells, and 96 forward and reverse primer mixtures were loaded into each assay wells (5 μl each). The IFC was then placed in the Juno™ Controller for automatic loading and mixing. After 90 minutes, the IFC was then transferred to the Biomark™ HD qPCR platform (Fluidigm). The cycling program consisted of Thermal Mix at 70°C for 40 min followed by 60°C for 30 s. Hot Start was 1 min at 95°C, followed by 30 cycles of denaturation at 96°C for 5 s, and annealing at 60°C for 20 s. Melting curves were collected between 60°C and 95°C with 1°C increments/3 s.

[1]Principal component analysis (PCA)

2.10. qPCR data processing and analysis

The Ct value of target genes was normalized to the housekeeping genes *Actb*, *Gapdh*, *Tbp*, and *Tfrc*. For hierarchical clustering, the gene expressions were calculated as number of transcripts with the housekeeping gene set as 10,000 transcripts. Mouse groups (columns) and genes (rows) were clustered using one minus Pearson correlation metric. For differential gene expression analysis, the fold-change value was calculated using the comparative threshold cycle method (ΔΔCt) with the WT mouse sample as control. Calculated data were presented as box-plots with averaged Ct from six animals as a data point. Student's t-test analysis was used to compare the differences between mutants and WT. All significant genes that were up- or down- regulated to the WT were plotted as Venn diagrams. To interpret the distinct and shared transcriptional modulation between *Adipor1*$^{-/-}$ and *Mfrp*^{rd6} mice, we used ConsensusPathDB (54) (http://cpdb.molgen.mpg.de/MCPDB) and uploaded the lists of genes that are increased or decreased in the mutant datasets (Supplemental Table 1). We picked the top 5 pathways (only 4 pathways found with the common downregulated genes) and plotted the percentage of genes within the total pathway population. All graphs were made using the Bio Vinci program (Bioturing Inc, San Diego, CA).

2.11. Statistics

The Kolmogorov-Smirnov test was employed to determine the assumption of normality for the SD-OCT measurements; an AR (1) as covariance structure was used for ERG measurements. A MANOVA test showed that differences existed among the retinal phosphatidylcholine (PC) data from the WT, *Adipor1*$^{-/-}$, and *Mfrp*^{rd6} animals; all p values < 0.0001 from Wilk's lambda, Pillai's Trace, Hotelling-Lawley Trace, and Roy's Greatest Root. Tukey-Kramer's multiple comparisons gave the final results (see Supplemental Table 2 for statistical details). * $p \leq 0.05$, ** $p \leq 0.01$, *** $p \leq 0.001$,**** $p \leq 0.0001$ throughout.

3. Results

3.1. PRC degeneration in Mfrp and Adipor1 mutant mice

Fundus imaging of 3-month-old *Mfrp*^{rd6} mice demonstrated a uniformly flecked retina similar to that found in the *Adipor1*$^{-/-}$ retina (12) and in human *fundus albipunctatus*. These white spots of uniform size were evenly distributed within the fundus and exhibited similar density in the *Mfrp*^{rd6} and *Adipor1*$^{-/-}$ retinas (Fig. 1A). Optical coherence tomography (OCT) revealed a reduction in outer retinal thickness; by three months of age, about 40% of PRC nuclei had been lost, and at five months only about 40% remained (Fig. 1B,C). Interestingly, the inner retina of the *Mfrp*^{rd6} appeared thicker (Fig. 1B,C). Overall, the *Mfrp*^{rd6} phenotype closely resembles the *Adipor1*$^{-/-}$ (12).

3.2. Retinal physiology is similarly impaired in Mfrp and Adipor1 mutants

ERGs were recorded from 2-month-old WT, *Mfrp*^{rd6} and *Adipor1*$^{-/-}$ during the onset of PRC death when the PRC layer began to decrease (Fig. 1B–D). ERGs obtained from light flashes ranging in intensity from 0.0001–10 cd·s/m^2 revealed a 50–75% decreased response in a-waves, for both the *Mfrp*^{rd6} and *Adipor1*$^{-/-}$ mice vs WT, indicating a reduction of PRC response. The b-wave was reduced by about 50% throughout, displaying an inner retinal

effect (largely bipolar cells). Interestingly, the dimmer light rod response in all mice plateaued through 0.005 cd·s/m^2 to 0.075 cd·s/m^2, followed by a similar rise in the brighter light cone response for all mice, indicating that reduced 22:6 affected both rods and cones (Fig. 1E). Since there is no apparent loss of inner retinal cells in these mutations, this suggests that the reduced signal originated in functionally impaired PRC.

3.3. Perturbations in the retinal lipidome containing highly unsaturated molecular species of phospholipids precedes PRC death in the Mfrp^{rd6} retina

22:6 is important for visual function and retinal homeostasis. However, this essential fatty acid must be obtained by diet, collected and packaged by the liver, and released into the circulation for targeted delivery to the RPE and PRC. Failure to achieve adequate delivery results in impaired photoreceptor function and eventual cell death.

MALDI IMS revealed relative molecular abundance (spectra from 400 to 1200 m/z) from scanned histological sections (Fig. 2A). MALDI analysis by positive ion mode of *Adipor1*$^{-/-}$, *Mfrp*^{rd6}, and WT retinas, demonstrated that the same phospholipids were present in the three genotypes, although the abundance of specific species within the mutant retinas were different from those of the WT. Analysis of MALDI sections revealed reliable identifying markers for the retinal layers (Fig. 2C–G): m/z 738 Uvea and RPE, m/z 756 PC(32:0) photoreceptor layer, m/z 760 PC(34:1) inner retina. m/z 900 PC(22:6/22:6), an n-3 phospholipid, labeled the PRCs of the WT, but was absent in both mutants; m/z 832 PC(20:4/18:0), an n-6 phospholipid, was present in all three animals, but was absent (greatly reduced) in the PRCs of the WT, indicating an n-3 phospholipid preference in WT PRCs. m/z 1046 PC(34:6/22:6), an n-3 VLC-PUFA-containing molecule, was prevalent at the outer edge of the PRC layer in the WT, but was absent in both mutants, indicating that the lack of 22:6 impaired the synthesis of the VLC-PUFA phospholipids.

LC-MS/MS-based retinal lipidomic analysis displays the quantitative PC molecular species distributions in bar graphs for the retina (top) and the RPE (bottom) (Fig. 2I). Clearly, 22:6-containing PCs are reduced in both *Adipor1*$^{-/-}$ and *Mfrp*^{rd6} retinas and RPE, especially PC(44:12) and PC(56:12), which are abundant in PRC outer segments (Fig. 2I, insets). The composition of the mass numbers used for retinal layer specification was determined by full fragmentation in negative ion mode (Fig. 2K and Supplemental Fig. 1). Matching of the peaks in positive and negative ion modes confirmed the identity of the molecules selected for retina specification (Fig. 2J). In our study, m/z 1104.6 (negative ion) and 1046.7 (positive ion) was identified as the m/z of VLC-PUFAs (Fig. 2F,J,K) that was not detectable in *Adipor1*$^{-/-}$ and *Mfrp*^{rd6}. These spectra indicate that a dysfunctional MFRP results in a remarkable altered retinal lipidome, and, based on the importance of 22:6 in retinal maintenance and function, suggests that reduction of 22:6 contributes to eventual PRC degeneration in the *Mfrp*^{rd6} mouse.

To further define differences in the retinal lipidome of the WT, *Mfrp*^{rd6}, and *Adipor1*$^{-/-}$, retinal sections were obtained and imaged by MALDI IMS. Total spectra from m/z 700 to m/z 1200 were collected from small retina regions for comparison (Fig. 3). A difference spectrum was then constructed by subtracting the *Adipor1*$^{-/-}$ or *Mfrp*^{rd6} profile from the WT profile (Fig. 3A,B). The resulting plots, while not quantitative, emphasized lipid

abundance, with the prevalent WT lipids (pointing up) and *Mfrp*^{rd6}, and *Adipor1*$^{-/-}$ lipids indicated as downward peaks. 22:6-containing PCs (m/z 828.61 PC(16:0/22:6) and m/z 856.64 PC(18:0/22:6)) were more prevalent in the WT retina; whereas the 20:4-containing PCs (m/z 804.6 PC(16:0/ 20:4) and m/z 832.64 PC(18:0/20:4)) were enhanced in mutant retinas. Analysis of VLC-PUFAs spectra (from m/z 1000 to m/z 1200) revealed them to be almost non-existent in both mutant retinas. Supplemental Table 3 depicts the more abundant phospholipid species revealed by the differential spectra of the WT, the *Mfrp*^{rd6}, and the *Adipor1*$^{-/-}$ retinas, emphasizing the lack of VLC-PUFA species in the mutants. To further highlight the retinal lipidome differences between *Adipor1*$^{-/-}$ and *Mfrp*^{rd6}, we generated differential spectrum of the two mutants (Fig. 3C). The relative amount of 22:6-containig PCs, although severely depleted in *Mfrp*^{rd6}, was still detectable compared to *Adipor1*$^{-/-}$. Supplemental Table 3 depicts the distribution of the more abundant phospholipid species revealed by the differential spectra of the *Mfrp*^{rd6} and the *Adipor1*$^{-/-}$ retinas. Overall, this comparison suggests that the 22:6-containing molecules are reduced in the *Mfrp*^{rd6} and *Adipor1*$^{-/-}$ retinas, while the 20:4-containing species are either retained or enhanced, indicating that products of n-3 fatty acid synthesis are reduced in the *Mfrp*^{rd6}, while the n-6 fatty acid pathway may be conserved.

3.4. VLC-PUFA-containing phosphatidylcholines are negligible in Mfrp^{rd6} mouse eyes

MALDI IMS suggests that abundance of 22:6-containing PCs in the *Mfrp*^{rd6} are drastically decreased (Fig. 2F,3B). Inability to take up and incorporate 22:6 in retina and RPE was discovered in the *Adipor1*$^{-/-}$ mouse (12). Similarly, in the *Mfrp*^{rd6}, there is almost complete loss of PC-containing fatty acids generated through the n-3 fatty acid synthesis pathway, especially the VLC-PUFAs (Fig. 2F,4,5). Since the *Mfrp*^{rd6} may have either lost the ability to take up 22:6 and/or synthesize PCs containing molecules elongated from 22:6 as in the *Adipor1* mutant, we investigated the overall retinal lipidome of 22:6-containing phospholipids in *Mfrp*^{rd6} retinas and RPE-eyecup. PC, phosphatidylethanolamine (PE), and phosphatidylserine (PS) molecular species in retinas and RPE-eyecups contain either 20:4 or 22:6, except PE(22:1/22:0) and PS(22:1/22:0) (Fig. 4,5). Overall, retinal PCs show that 20:4-containing species are more abundant in the mutants, while 22:6-containing species are highly reduced (Fig. 4). In PEs, 20:4-containing species are higher in the mutants, but this phospholipid with a single 22:6 ((e.g., PE(16:0/22:6) and PE(18:0/22:6)) is not different from WT. However, PE(22:6/22:6) and PE(24:6/22:6) are greatly reduced in the mutants (Fig. 4) At the same time, PS shows a large increase in single-22:6-containing species (PS(16:0/22:6) and PS(18:0/22:6)), while PS(22:6/22:6) and PS(24:6/22:6) are greatly reduced as in the PEs (Fig. 4). In the RPE-eyecup, single 22:6 containing species (16:0/22:6, 18:0/22:6) for both PC and PE are more abundant in the mutants (Fig. 5), but the 22:6/22:6 and 24:6/22:6 species are greatly reduced as they are in retinas. The 22:6-containg PSs in the RPE-eyecups were not detectable.

Principal Component Analysis (PCA) of WT and mutant retinas and RPE-eyecups show good separation, particularly with retina (Fig. 6A). Hierarchical clustering reveals two major clusters in retina (Fig. 6B) and RPE-eyecup (Fig. 6C), with red and blue indicating increased and decreased abundance, respectively. A Venn diagram (Fig. 6D) depicts the overlap of

significant differentially occurring PCs across strains and tissues. The numbers in each oval show the number of PC species statistically different vs WT.

3.5. Phosphatidylcholines containing LC-PUFAs with 4–7 double bonds are enhanced in Mfrp^{rd6} and Adipor1$^{-/-}$ mice.

While there is a reduction of VLC-PUFAs in the mutants, even within PCs containing fewer than 10 double bonds, additional LC-MS/MS analyses of retinas and RPE-eyecups revealed increases in some 4–7 double bond, 50–58 C PC molecular species (Supplemental Fig. 3). These increases, which may be compensatory, were observed in retinas and RPE-eyecups of both *Mfrp* and *Adipor1* mutants. However, since PRCs were eventually lost, compensatory replacement with alternate PC species was only a temporary fix, signifying a potential transient mechanism to sustain the retinal lipidome until adequate 22:6 could be achieved.

3.6. VLC-PUFAs abundance and Elovl4 expression decline in Mfrp^{rd6} retinas

Functional *Mfrp* gene yields a retinal lipidome rich in PC species (Fig. 6) required for *Elovl4* expression. We found reduced *Elovl4* expression in the *Mfrp*^{rd6} RPE-eyecups and retina (Fig. 7C, Supplemental Fig. 6A), which further explains the decreased abundance of VLC-PUFAs that we found.

3.7. Genes signatures of pro-inflammatory signaling pathways are increased and genes encoding proteins for PRC function are decreased in AdipoR1$^{-/-}$ and Mfrp^{rd6}

Mutation of *Mfrp* or *Adipor1* affects differentially signaling pathways leading to PRC death, as revealed by RT-qPCR analysis of the expression of 88 candidate genes in retina and RPE-eyecups. Target genes were selected for their function in the visual system and their role in inflammatory and immune system pathways. We found a higher hierarchical clustering of the selected genes for retina (Fig. 7A) compared to the RPE-eyecup (Supplemental Fig. 4), likely because the RPE-eyecup is less sensitive to the *Mfrp* or *Adipor1* mutation, as opposed to PRCs, which subsequently degenerates. Box-plots show the expression range of individual genes with the most significant fold-change in retina (Fig. 7B) and RPE-eyecup (Fig. 7C) across the three different genotypes (*Mfrp*^{rd6}, *Adipor1*$^{-/-}$ and WT). Genes with higher fold-change differences in retina were linked to inflammatory pathways: *Birc3*, *Pycard*, *Casp1*, *Il1b*, *Fas*, *Naip*, and *Tnf*. Interestingly, genes that are part of the pyroptosis cell death pathway, such as *Casp1* and *Pycard*, were upregulated more than 4- and 3-fold, respectively, in mutants. Next, we followed the expression of genes associated with visual function, and linked to retinopathies when dysregulated. ROM1 is part of the protein complex containing PRPH2 that contributes to PRC disk morphogenesis. We found a 3-fold downregulation of *Rom1* in both mutants (Fig. 7B), and although attenuated, the mutant retinas also displayed a downward regulation of *Prph2* expression (Supplemental Fig. 5A). *Gfap*, a marker of reactive gliosis in the Müller glia cells, was upregulated 5-fold in *Adipor1*$^{-/-}$ and more than 3-fold in *Mfrp*^{rd6} (Fig. 7B). In the RPE-eyecup, there were only a few genes that displayed more than a 2-fold change between mutants and WT. Among these genes, *Elovl4* (1.5- to 2-fold) and *Reep6* (3-fold) were decreased in mutants, while genes associated with inflammatory pathways, *Fadd* and *Tnf*, were increased 2-fold in *Adipor1*$^{-/-}$ RPE-eyecups only (Fig. 7C). We investigated the classical signal transduction pathway via Adiponectin receptors, ADIPOR1 and ADIPOR2, which modulates different biological

events such as steroidogenesis, glucose uptake, cell survival, fatty acid oxidation, vasodilatation, and cytoprotection (39). Although most of the candidate genes did not have their FC <−2 or >2 (except for *Adipor1* in the *Adipor1*$^{-/-}$ dataset), they displayed differences compared to the WT. *Adipor1* expression was decreased by 1.5-fold in the retina and 1.4-fold in the RPE-eyecup of *Mfrp*^{rd6} (Supplemental Fig. 5). *Adipor2* was reduced in *Adipor1*$^{-/-}$ retina and RPE-eyecup, possibly as a compensatory way to respond to *Adipor1* deletion (Supplemental Fig. 5). Interestingly, *Mfrp* expression was not significantly affected in either the retina or RPE-eyecup of *Adipor1*$^{-/-}$, suggesting a feedback loop for transcriptional regulation of *Adipor1* by MFRP (Supplemental Fig. 7). Overall, a downregulation of genes was linked to visual function in the retina of both mutants (Supplemental Fig. 6A), implying that the dysregulation of ADIPOR1 and MFRP have direct impact on the physiology of the PRC and their survival.

In *Adipor1*$^{-/-}$ and *Mfrp*^{rd6} retina datasets, seven and six distinct genes, respectively, were upregulated (Fig. 7D). To highlight the particularity of each mutant and to understand if they follow a specific degenerative pathway, we looked at the over- representation of candidate genes in enriched pathway-based sets (Fig. 7E–H). The most highly represented biological activities enriched in the mutants compared to the WT, mainly involved response to inflammation and cellular processes for programmed cell death. The highest score of over-representation of candidate genes upregulated in *Adipor1*$^{-/-}$ dataset belonged to JNK (c-Jun kinases) phosphorylation and activation mediated by the activated human TAK1 pathway (Fig. 7E), while upregulated candidates in the *Mfrp*^{rd6} dataset belonged mainly to the NOD-like receptor signaling pathway (Fig. 7F). The common upregulated candidate genes (Supplemental Table 1) in *Adipor1*$^{-/-}$ and *Mfrp*^{rd6} datasets are mainly represented within the AIM2 inflammasome pathway (Fig. 7G).

Regarding the downregulated candidates, we found six unique upregulated genes in the *Adipor1*$^{-/-}$ dataset, while there were none in the *Mfrp*^{rd6} dataset (Fig. 7D). The list of these genes did not hit any enriched pathway-based sets, most likely because of the reduced list size. Common candidate genes downregulated in mutant datasets had the highest over-representation score for the neural retinal development pathway (Fig. 7H); these candidate genes have a function in the development and function of PRC, thus, ADIPOR1 and MFRP are essential to the maintenance of PRC homeostasis by acting directly or indirectly on effectors for cellular integrity.

4. Discussion

A central question regarding onset and progression of retinal degenerative diseases is how acquisition of key molecules in the retinal lipidome takes place, and how they sustain transcriptomic programs for retinal function. To address this question, this study used sensitive and specific mass spectrometry-based molecular imaging (MALDI IMS) for mapping the untargeted *in situ* spatial distribution of molecular species of phospholipids, complemented with LC-MS/MS quantification and detailed characterization, with OCT imaging and analysis of electroretinograms (ERG) to assess retina structure and function. Additionally, transcriptomic approaches have allowed us to define gene signatures involved in PRC degeneration in the *Mfrp*^{rd6} mouse, and to establish analogies and differences with

Adipor1$^{-/-}$ mouse, particularly preceding retinal degeneration. These findings have revealed novel necessary molecular events for PRC function.

Mfrp^{rd6} displays characteristics similar to those expressed in human *retinitis punctata albescens* (7, 9). Subretinal flecks also appear across the retina in this mouse, corresponding to accumulation of macrophages within the subretinal space, and this phenotypic characteristic is also evident in the *Adipor1*$^{-/-}$ retinas. While a detailed timeline has not been established for these mutants, histology demonstrated the accumulation of autofluorescence of undigested outer segments within the RPE, and OCT analysis revealed a progressive decline in the outer retina thickness as a result of PRC loss (12). Outer retinas (the PRC layer) of both mutants show a reduction from the normal to about 40% at one month with progressive loss up to 5 months, the *Adipor1*$^{-/-}$ declining more rapidly. Moreover, the ERG declined by P25, indicating slow loss of function (12), with both mutant ERGs reduced to about 50% at 2 months. Differences in lipids among 3 month mutants and WT are described, but it is not known whether these differences are unchanged from birth in the mutants or are a result of an ongoing restructuring and compensation. An earlier study demonstrated that key retinal proteins were depressed and that rhodopsin was depleted prior to PRC death by P21 in the *Mfrp*^{rd6} mice (10). Changes associated with the RPE cells in the *Mfrp*^{rd6} mice have also been noted (9, 40). Developing *Mfrp*^{rd6} mice show reduced RPE microvilli, altered PRC inner segments, and disorganized outer segments, as well as impaired phagocytosis of PRC apical outer segments (40). Conversely, in RPE cell cultures, an increased number of RPE microvilli occur in the *Mfrp* mutants (9). Alterations in microvilli formation, density, and/or distribution would affect outer segment shedding, disrupt the process of membrane disposal by the RPE, and upset the retinal lipidome and PRC homeostasis.

MFRP has been localized in the RPE apical membrane and along the entire length of the RPE microvilli, as well as in PRC inner segments. *MFRP* is expressed as a dicistronic transcript with the *C1q tumor necrosis factor-related protein-5* (*C1QTNF5*/*CTRP*5) gene (2, 41, 42), which is associated with cell adhesion and basement membranes (43) in the RPE and ciliary body (44), and the MFRP level is inversely proportional to CTRP5 expression (45). β-actin is increased in MFRP-deficient cells and in cells overexpressing CTRP5, and MFRP affects actin polymerization, RPE cell adhesion, and microvilli morphology (45). CTRP5 is also localized in the RPE microvilli (44), and CTRP5 molecules form multimers in adjacent RPE cells with their collagen domains binding to collagen receptors in the membranes and their globular heads interacting to enhance RPE cell-cell adhesion (46). This has suggested a potential interaction with actin filaments (47) at this level. An interaction here could be diminished since the *MFRP*^{rd6} mice have reduced/distorted RPE microvilli (9, 40), which could reduce interdigitation with outer segments and impede 22:6 trafficking.

22:6 is reduced in both retina and RPE. The RPE regulates 22:6 uptake from the choriocapillaris, but their altered microvilli in the MFRP^{rd6} mice suggest that redistribution of the 22:6 from the RPE to photoreceptors may be impeded or prevented. Eventually, with no or little 22:6 to form the neuroprotective compounds, the presence/accumulation of unmitigated stress would trigger an inflammatory response. Thus, arachidonic acid (20:4) is

noticeably increased in both mutants, while it is notably less in the healthy WT mice, especially as compared with the abundance of 22:6 in the WT.

Healthy RPE cells are necessary for PRC integrity, recycling 22:6 from phagosomes back to the PRCs for synthesis of new disk membranes (16, 40). Thus, RPE cells regulate 22:6 trafficking to the PRC, and impediments to this process limits the availability of 22:6 for elongation to VLC-PUFAs and for the synthesis of NPD1 and the ELV neuroprotectants, diminishing the ability to counter unmitigated oxidative stress and retinal homeostatic upset (28). The availability of this dual protective mechanism in which stress triggers 22:6 release and its conversion to NPD1, as well as the VLC-PUFAs and their conversion to ELV (28), is important to sustain PRCs. Therefore, we monitored 22:6 accumulation and elongation to VLC-PUFAs in retina by observing the distribution of n-3 PC(44:12), containing two 22:6 molecules, and n-6 PC(38:4), containing (18:0/20:4). In those same retinas MALDI imaging showed that PC(56:12), containing the n-3 VLC-PUFAs 34:6 and 22:6, was localized within the outer PRC layer in WT retinas, but was absent in both mutant retinas. Conversely, the n-6 PC(38:4) was abundant within the PRC. Also, VLC-PUFAs were undetectable in the MALDI spectra of the *Adipor1*$^{-/-}$ and *rd6* mice. Our data show that depressed PRC 22:6 n-3 in both mutants was accompanied by a compensatory response where less prevalent n-6 molecules were increased in the photoreceptor layer. Absence of 22:6 and the VLC-PUFAs, therefore, results in an increased n-6/n-3 ratio in the *Adipor1*$^{-/-}$ and *rd6* retinas, as similarly noted in AMD donor retinas (48). This creates a 20:4 n-6-enriched phospholipid environment which likely results in a proinflammatory condition, which contributes to the onset of PRC dysfunction. Since the n-3 VLC-PUFAs are released from their PC molecules upon unmitigated stress, and converted to protective elovanoids (ELVs) (37), absence of this pathway favors PRC degeneration.

We suggest that the absence of 22:6, and, therefore, the lack of VLC-PUFAs, in the *Mfrp*^{rd6} and *Adipor1*$^{-/-}$ mice leads to transcriptomic modifications, which then trigger an increase of pro-inflammatory genes and a decrease of genes that are critical for visual system function. Transcriptome analysis provides insight into the relationship between *Mfrp* and *Adipor1*. Our gene signature shows that the JNK phosphorylation and activation mediated by the activated TAK1 pathway is initiated in *Adipor1*$^{-/-}$ retina. The induction of this pathway could be due to the relative abundance of arachidonoyl groups in phospholipids in *Adipor1*$^{-/-}$ retina that provides substrate for COX2 activation by c-Jun kinases to foster the formation of pro-inflammatory effectors that ultimately contribute to triggering cell death pathways (49). On the other hand, the favored pathway for *Mfrp*^{rd6} is NOD-like receptor signaling. Free radicals and lipid peroxidation products in the retina activate this pathway. This is facilitated because the recycling by the RPE is altered in *Mfrp*^{rd6}, enabling accumulation of these harmful molecules that in turn could establish a stress-prone environment for PRC. As a consequence, the activation of the NOD-like receptor signaling pathway takes place. It is probable that although there is a distinct induction of inflammatory pathways in *Adipor1*$^{-/-}$ and *Mfrp*^{rd6}, there is eventually a convergence of pathways and, in this case, the predicted AIM2 inflammasome signaling, which would then activate apoptotic and pyroptotic signals following the activation of caspase-8 and −1 (50).

Taken together, our study demonstrates that the *Mfrp* mutation resembles the *Adipor1* mutation on multiple levels, with some transcriptome differences: 1) phenotypically, the deletion of these proteins leads to flecked retina and slow PRC death onset; 2) functionally, the mutations express the same degree of ERG attenuation; 3) both mutants clearly demonstrate the inability to take up and incorporate 22:6 in the RPE and PRC, which results in remarkable changes in the retinal lipidome; and 4) although the gene signature shows that both mutants are activated by signaling pathways involving proinflammatory cytokines, we found that each of these pathways have distinct features. Moreover, our results highlight the critical role of MFRP and ADIPOR1 in preserving PRC integrity through regulation of enrichment and distribution of 22:6 which, importantly, affects the synthesis of VLC-PUFAs that provide the precursors for the neuroprotective ELVs. Hence, the maintenance of a balanced 22:6 retinal lipidome relies on MFRP and ADIPOR1, acting to ensure proper acquisition and distribution of key lipids from the RPE to the PRC, these events are necessary to sustain function in early stages of AMD and of other retinal degenerative deceases.

Supplementary Material

Refer to Web version on PubMed Central for supplementary material.

Acknowledgments

This work was supported by National Institutes of Health (NIH) grants R01 EY005121 (National Eye Institute) and P30 GM103340 (National Institute of General Medical Sciences) to NGB, the Eye, Ear, Nose & Throat Foundation of New Orleans, and, in part, by the Research to Prevent Blindness, New York, NY. We thank Thang Pham for technical assistance with the transcriptomic analysis, and Jessica Heap for her help with the lipids Venn diagram figure.

List of Nonstandard Abbreviations

AdipoR1	Adiponectin Receptor 1
AMD	age-related macular degeneration
C1QTNF5/CTRP5	C1q tumor necrosis factor-related protein-5
DHB	dihydroxybenzoic acid
ELOVL4	ELOngation of Very Long chain fatty acids-4
ELVs	elovanoids
EPA	eicosapentaenoic acid
ERG	electroretinograms
JNK	c-Jun kinases
MALDI IMS	mass spectrometry-based molecular imaging
MALDI IMS	Matrix-assisted laser desorption/ionization imaging mass spectrometry

MFRP	Membrane-type Frizzled-Related Protein
NPD1	neuroprotectin D1
OCT	optical coherence tomography
PC	phosphatidylcholine
PCA	Principal Component Analysis
PE	phosphatidylethanolamine
PRC	photoreceptor
PS	phosphatidylserine
RPE	retinal pigment epithelium
SD-OCT	Spectral Domain-Optical Coherence Tomography
UOS	uncompensated oxidative stress
VLC-PUFAs	very long-chain polyunsaturated fatty acids
VLC-SFAs	very long-chain saturated fatty acids
WT	wild-type

7. References

1. Katoh M (2001) Molecular cloning and characterization of MFRP, a novel gene encoding a membrane-type Frizzled-related protein. Biochem. Biophys. Res. Commun 282, 116–123 [PubMed: 11263980]
2. Kameya S, Hawes NL, Chang B, Heckenlively JR, Naggert JK, and Nishina PM (2002) Mfrp, a gene encoding a frizzled related protein, is mutated in the mouse retinal degeneration 6. Hum. Mol. Genet 11, 1879–1886 [PubMed: 12140190]
3. Van Raay TJ and Vetter ML (2004) Wnt/frizzled signaling during vertebrate retinal development. Dev. Neurosci 26, 352–358 [PubMed: 15855764]
4. Ayala-Ramirez R, Graue-Wiechers F, Robredo V, Amato-Almanza M, Horta-Diez I, and Zenteno JC (2006) A new autosomal recessive syndrome consisting of posterior microphthalmos, retinitis pigmentosa, foveoschisis, and optic disc drusen is caused by a MFRP gene mutation. Mol. Vis 12, 1483–1489 [PubMed: 17167404]
5. Fogerty J and Besharse JC (2014) Subretinal infiltration of monocyte derived cells and complement misregulation in mice with AMD-like pathology. Adv. Exp. Med. Biol 801, 355–363 [PubMed: 24664718]
6. Collery RF, Volberding PJ, Bostrom JR, Link BA, and Besharse JC (2016) Loss of Zebrafish Mfrp Causes Nanophthalmia, Hyperopia, and Accumulation of Subretinal Macrophages. Invest. Ophthalmol. Vis. Sci 57, 6805–6814 [PubMed: 28002843]
7. Hawes NL, Chang B, Hageman GS, Nusinowitz S, Nishina PM, Schneider BS, Smith RS, Roderick TH, Davisson MT, and Heckenlively JR (2000) Retinal degeneration 6 (rd6): a new mouse model for human retinitis punctata albescens. Invest. Ophthalmol. Vis. Sci 41, 3149–3157 [PubMed: 10967077]
8. Krill Alex E. (1977) Flecked retina diseases In Hereditary Retinal and Choroidal Dystrophies (Krill AE and Archer DB, eds) vol. II, pp. 739–824, Harper & Row, New York

9. Fogerty J and Besharse JC (2011) 174delG mutation in mouse MFRP causes photoreceptor degeneration and RPE atrophy. Invest. Ophthalmol. Vis. Sci 52, 7256–7266 [PubMed: 21810984]
10. Sluch VM, Banks A, Li H, Crowley MA, Davis V, Xiang C, Yang J, Demirs JT, Vrouvlianis J, Leehy B, Hanks S, Hyman AM, Aranda J, Chang B, Bigelow CE, and Rice DS (2018) ADIPOR1 is essential for vision and its RPE expression is lost in the Mfrprd6 mouse. Sci Rep 8, 14339 [PubMed: 30254279]
11. Velez G, Tsang SH, Tsai Y-T, Hsu C-W, Gore A, Abdelhakim AH, Mahajan M, Silverman RH, Sparrow JR, Bassuk AG, and Mahajan VB (2017) Gene Therapy Restores Mfrp and Corrects Axial Eye Length. Sci Rep 7, 16151 [PubMed: 29170418]
12. Rice DS, Calandria JM, Gordon WC, Jun B, Zhou Y, Gelfman CM, Li S, Jin M, Knott EJ, Chang B, Abuin A, Issa T, Potter D, Platt KA, and Bazan NG (2015) Adiponectin receptor 1 conserves docosahexaenoic acid and promotes photoreceptor cell survival. Nature Communications 6, 6228
13. Zhang J, Wang C, Shen Y, Chen N, Wang L, Liang L, Guo T, Yin X, Ma Z, Zhang B, and Yang L (2016) A mutation in ADIPOR1 causes nonsyndromic autosomal dominant retinitis pigmentosa. Hum. Genet 135, 1375–1387 [PubMed: 27655171]
14. Xu M, Eblimit A, Wang J, Li J, Wang F, Zhao L, Wang X, Xiao N, Li Y, Wong L-JC, Lewis RA, and Chen R (2016) ADIPOR1 Is Mutated in Syndromic Retinitis Pigmentosa. Hum. Mutat 37, 246–249 [PubMed: 26662040]
15. Kaarniranta K, Paananen J, Nevalainen T, Sorri I, Seitsonen S, Immonen I, Salminen A, Pulkkinen L, and Uusitupa M (2012) Adiponectin receptor 1 gene (ADIPOR1) variant is associated with advanced age-related macular degeneration in Finnish population. Neurosci. Lett 513, 233–237 [PubMed: 22387454]
16. Rodriguez de Turco EB, Gordon WC, and Bazan NG (1991) Rapid and selective uptake, metabolism, and cellular distribution of docosahexaenoic acid among rod and cone photoreceptor cells in the frog retina. J. Neurosci 11, 3667–3678 [PubMed: 1834810]
17. Metherel AH, Irfan M, Chouinard-Watkins R, Trépanier M-O, Stark KD, and Bazinet RP (2019) DHA Cycling Halves the DHA Supplementation Needed to Maintain Blood and Tissue Concentrations via Higher Synthesis from ALA in Long-Evans Rats. J. Nutr 149, 586–595 [PubMed: 30715388]
18. Scott BL and Bazan NG (1989) Membrane docosahexaenoate is supplied to the developing brain and retina by the liver. PNAS 86, 2903–2907 [PubMed: 2523075]
19. Bazan NG, Molina MF, and Gordon WC (2011) Docosahexaenoic acid signalolipidomics in nutrition: significance in aging, neuroinflammation, macular degeneration, Alzheimer's, and other neurodegenerative diseases. Annu. Rev. Nutr 31, 321–351 [PubMed: 21756134]
20. Fliesler SJ and Anderson RE (1983) Chemistry and metabolism of lipids in the vertebrate retina. Prog. Lipid Res 22, 79–131 [PubMed: 6348799]
21. Aveldaño MI (1987) A novel group of very long chain polyenoic fatty acids in dipolyunsaturated phosphatidylcholines from vertebrate retina. J. Biol. Chem 262, 1172–1179 [PubMed: 3805015]
22. Bazan NG (2006) Cell survival matters: docosahexaenoic acid signaling, neuroprotection and photoreceptors. Trends Neurosci 29, 263–271 [PubMed: 16580739]
23. Wassall SR, Leng X, Canner SW, Pennington ER, Kinnun JJ, Cavazos AT, Dadoo S, Johnson D, Heberle FA, Katsaras J, and Shaikh SR (2018) Docosahexaenoic acid regulates the formation of lipid rafts: A unified view from experiment and simulation. Biochim Biophys Acta Biomembr 1860, 1985–1993 [PubMed: 29730243]
24. Soubias O, Teague WE, and Gawrisch K (2006) Evidence for specificity in lipid-rhodopsin interactions. J. Biol. Chem 281, 33233–33241 [PubMed: 16959786]
25. Sánchez-Martín MJ, Ramon E, Torrent-Burgués J, and Garriga P (2013) Improved conformational stability of the visual G protein-coupled receptor rhodopsin by specific interaction with docosahexaenoic acid phospholipid. Chembiochem 14, 639–644 [PubMed: 23447332]
26. Litman BJ, Niu SL, Polozova A, and Mitchell DC (2001) The role of docosahexaenoic acid containing phospholipids in modulating G protein-coupled signaling pathways: visual transduction. J. Mol. Neurosci 16, 237–242; discussion 279–284 [PubMed: 11478379]
27. Mitchell DC, Niu S-L, and Litman BJ (2003) Enhancement of G protein-coupled signaling by DHA phospholipids. Lipids 38, 437–443 [PubMed: 12848291]

28. Bazan NG (2018) Docosanoids and elovanoids from omega-3 fatty acids are pro-homeostatic modulators of inflammatory responses, cell damage and neuroprotection. Mol. Aspects Med 64, 18–33 [PubMed: 30244005]
29. Lagali PS, Liu J, Ambasudhan R, Kakuk LE, Bernstein SL, Seigel GM, Wong PW, and Ayyagari R (2003) Evolutionarily conserved ELOVL4 gene expression in the vertebrate retina. Invest. Ophthalmol. Vis. Sci 44, 2841–2850 [PubMed: 12824221]
30. Hopiavuori BR, Anderson RE, and Agbaga M-P (2018) ELOVL4: Very long-chain fatty acids serve an eclectic role in mammalian health and function. Progress in Retinal and Eye Research
31. Suh M and Clandinin MT (2005) 20:5n-3 but not 22:6n-3 is a preferred substrate for synthesis of n-3 very-long- chain fatty acids (C24-C36) in retina. Curr. Eye Res 30, 959–968 [PubMed: 16282130]
32. Yu M, Benham A, Logan S, Brush RS, Mandal MNA, Anderson RE, and Agbaga M-P (2012) ELOVL4 protein preferentially elongates 20:5n3 to very long chain PUFAs over 20:4n6 and 22:6n3. J. Lipid Res 53, 494–504 [PubMed: 22158834]
33. Agbaga M-P, Mandal MNA, and Anderson RE (2010) Retinal very long-chain PUFAs: new insights from studies on ELOVL4 protein. J. Lipid Res 51, 1624–1642 [PubMed: 20299492]
34. Oresti GM, Ayuza Aresti PL, Gigola G, Reyes LE, and Aveldaño MI (2010) Sequential depletion of rat testicular lipids with long-chain and very long-chain polyenoic fatty acids after X-ray-induced interruption of spermatogenesis. J. Lipid Res 51, 2600–2610 [PubMed: 20529883]
35. Cameron DJ, Tong Z, Yang Z, Kaminoh J, Kamiyah S, Chen H, Zeng J, Chen Y, Luo L, and Zhang K (2007) Essential role of Elovl4 in very long chain fatty acid synthesis, skin permeability barrier function, and neonatal survival. Int. J. Biol. Sci 3, 111–119 [PubMed: 17304340]
36. Monroig Ó, Rotllant J, Cerdá-Reverter JM, Dick JR, Figueras A, and Tocher DR (2010) Expression and role of Elovl4 elongases in biosynthesis of very long-chain fatty acids during zebrafish Danio rerio early embryonic development. Biochimica et Biophysica Acta (BBA) - Molecular and Cell Biology of Lipids 1801, 1145–1154 [PubMed: 20601113]
37. Jun B, Mukherjee PK, Asatryan A, Kautzmann M-A, Heap J, Gordon WC, Bhattacharjee S, Yang R, Petasis NA, and Bazan NG (2017) Elovanoids are novel cell-specific lipid mediators necessary for neuroprotective signaling for photoreceptor cell integrity. Scientific Reports 7, 5279 [PubMed: 28706274]
38. Hollyfield JG, Bonilha VL, Rayborn ME, Yang X, Shadrach KG, Lu L, Ufret RL, Salomon RG, and Perez VL (2008) Oxidative damage-induced inflammation initiates age-related macular degeneration. Nat. Med 14, 194–198 [PubMed: 18223656]
39. Mao X, Kikani CK, Riojas RA, Langlais P, Wang L, Ramos FJ, Fang Q, Christ-Roberts CY, Hong JY, Kim R-Y, Liu F, and Dong LQ (2006) APPL1 binds to adiponectin receptors and mediates adiponectin signalling and function. Nat. Cell Biol 8, 516–523 [PubMed: 16622416]
40. Won J, Smith RS, Peachey NS, Wu J, Hicks WL, Naggert JK, and Nishina PM (2008) Membrane frizzled-related protein is necessary for the normal development and maintenance of photoreceptor outer segments. Vis. Neurosci 25, 563–574 [PubMed: 18764959]
41. Hayward C, Shu X, Cideciyan AV, Lennon A, Barran P, Zareparsi S, Sawyer L, Hendry G, Dhillon B, Milam AH, Luthert PJ, Swaroop A, Hastie ND, Jacobson SG, and Wright AF (2003) Mutation in a short-chain collagen gene, CTRP5, results in extracellular deposit formation in late-onset retinal degeneration: a genetic model for age-related macular degeneration. Hum. Mol. Genet 12, 2657–2667 [PubMed: 12944416]
42. Mandal MNA, Vasireddy V, Jablonski MM, Wang X, Heckenlively JR, Hughes BA, Reddy GB, and Ayyagari R (2006) Spatial and temporal expression of MFRP and its interaction with CTRP5. Invest. Ophthalmol. Vis. Sci 47, 5514–5521 [PubMed: 17122143]
43. Reference GH C1QTNF5 gene. Genetics Home Reference
44. Mandal MNA, Vasireddy V, Reddy GB, Wang X, Moroi SE, Pattnaik BR, Hughes BA, Heckenlively JR, Hitchcock PF, Jablonski MM, and Ayyagari R (2006) CTRP5 is a membrane-associated and secretory protein in the RPE and ciliary body and the S163R mutation of CTRP5 impairs its secretion. Invest. Ophthalmol. Vis. Sci 47, 5505–5513 [PubMed: 17122142]
45. Li Y, Wu W-H, Hsu C-W, Nguyen HV, Tsai Y-T, Chan L, Nagasaki T, Maumenee IH, Yannuzzi LA, Hoang QV, Hua H, Egli D, and Tsang SH (2014) Gene therapy in patient-specific stem cell

lines and a preclinical model of retinitis pigmentosa with membrane frizzled-related protein defects. Mol. Ther 22, 1688–1697 [PubMed: 24895994]

46. Tu X and Palczewski K (2014) The macular degeneration-linked C1QTNF5 (S163) mutation causes higher-order structural rearrangements. J. Struct. Biol 186, 86–94 [PubMed: 24531000]
47. Dinculescu A, Min S-H, Deng W-T, Li Q, and Hauswirth WW (2014) Gene therapy in the rd6 mouse model of retinal degeneration. Adv. Exp. Med. Biol 801, 711–718 [PubMed: 24664762]
48. Liu A, Chang J, Lin Y, Shen Z, and Bernstein PS (2010) Long-chain and very long-chain polyunsaturated fatty acids in ocular aging and age-related macular degeneration. J. Lipid Res. 51, 3217–3229 [PubMed: 20688753]
49. Hunot S, Vila M, Teismann P, Davis RJ, Hirsch EC, Przedborski S, Rakic P, and Flavell RA (2004) JNK-mediated induction of cyclooxygenase 2 is required for neurodegeneration in a mouse model of Parkinson's disease. Proc. Natl. Acad. Sci. U.S.A 101, 665–670 [PubMed: 14704277]
50. Sagulenko V, Thygesen SJ, Sester DP, Idris A, Cridland JA, Vajjhala PR, Roberts TL, Schroder K, Vince JE, Hill JM, Silke J, and Stacey KJ (2013) AIM2 and NLRP3 inflammasomes activate both apoptotic and pyroptotic death pathways via ASC. Cell Death Differ. 20, 1149–1160 [PubMed: 23645208]
51. Mattapallil MJ, Wawrousek EF, Chan C-C, Zhao H, Roychoudhury J, Ferguson TA, and Caspi RR (2012) The Rd8 mutation of the Crb1 gene is present in vendor lines of C57BL/6N mice and embryonic stem cells, and confounds ocular induced mutant phenotypes. Invest. Ophthalmol. Vis. Sci 53, 2921–2927 [PubMed: 22447858]
52. Ferguson LR, Dominguez JM, Balaiya S, Grover S, and Chalam KV (2013) Retinal Thickness Normative Data in Wild-Type Mice Using Customized Miniature SD-OCT. PLoS ONE 8, e67265 [PubMed: 23826252]
53. Liebisch G, Vizcaíno JA, Köfeler H, Trötzmüller M, Griffiths WJ, Schmitz G, Spener F, and Wakelam MJO (2013) Shorthand notation for lipid structures derived from mass spectrometry. J. Lipid Res 54, 1523–1530 [PubMed: 23549332]
54. Kamburov A, Stelzl U, Lehrach H, and Herwig R (2013) The ConsensusPathDB interaction database: 2013 update. Nucleic Acids Res 41, D793–800 [PubMed: 23143270]
55. Hankin JA, Barkley RM, Murphy RC. Sublimation as a Method of Matrix Application for Mass Spectrometric Imaging. J Am Soc Mass Spectrom 2007; 18 (9): 1646–1652. [PubMed: 17659880]

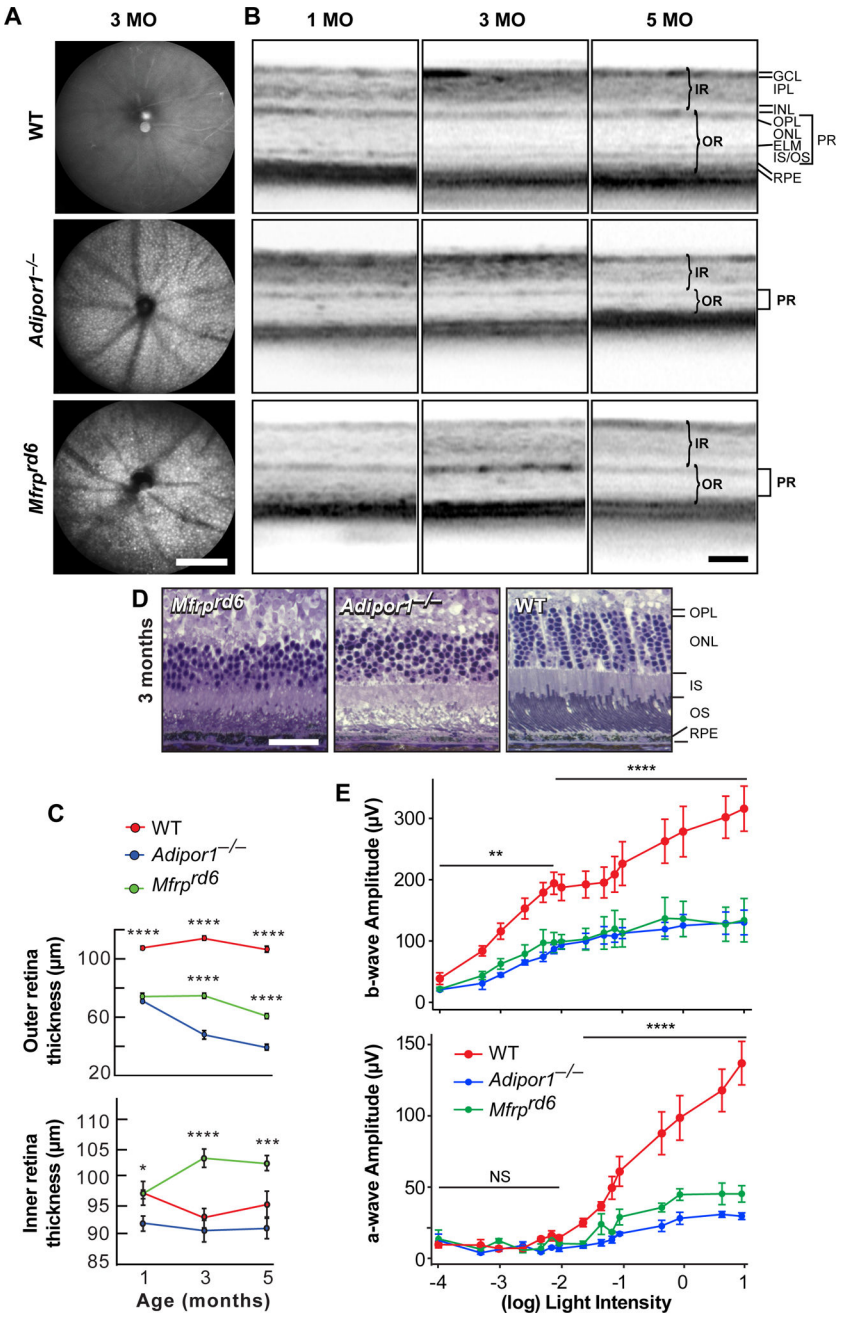

Fig. 1.

Progressive PRC degeneration is similar in *Mfrp*^{rd6} and *Adipor1* mutants. **(A)** Fundus imaging revealed dense, evenly distributed white, punctate spots deep within 3-month-old mouse retinas, as observed in the *Adipor1*$^{-/-}$ mouse. Images are representative of 4 mice. **(B)** Optical coherence tomography (OCT) for 1, 3, and 5-month-old *Mfrp*^{rd6} and *Adipor1*$^{-/-}$ retinas demonstrated a gradual reduction in the photoreceptor layer thickness when compared to wild-type (WT) mice. **(C)** The outer retina (OR, photoreceptors + RPE) thickness in both mutants at 1 month of age is reduced compared to the WT retina; the *Mfrp*^{rd6} decreases slightly by 5 months, while the *Adipor1*$^{-/-}$ OR continually decreases. The

inner retinas (IR) remain unchanged for the WT and the *Adipor1*$^{-/-}$, however the *Mfrp*^{rd6} IR is thicker at 3 and 5 months. Error bars represent SEM of 3 individuals. **(D)** Histological sections illustrating cellular morphology and changes in thickness of the *Mfrp*^{rd6} and *Adipor1*$^{-/-}$ photoreceptor layers, relative to WT mice, especially evident in the reduction of photoreceptors nuclei within the ONL. Each image is representative of 3 mice. **(E)** a- and b-wave electroretinographic (ERG) responses of 2-month old animals, to increasing intensities of light (cd•s/m^2). *Mfrp*^{rd6} and *Adipor1*$^{-/-}$ retinal responses were reduced by approximately 75% and 50%, respectively, from those of WT mice. Generally, both mutant mice displayed similar reductions. Error bars represent SEM of 3 individuals. GCL, ganglion cell layer; IPL, Inner Plexiform Layer; INL, Inner Nuclear Layer; OPL, Outer Plexiform Layer; ONL; Outer Nuclear Layer; ELM, External Limiting Membrane; IS/OS, Inner/Outer Segments; RPE, Retinal Pigment Epithelium; IR, inner retina; OR, outer retina; PR, photoreceptors. Magnification bars: **(A)** 200 μm; **(B)** 100 μm; **(D)** 100 μm. * $p \leq 0.05$, ** $p \leq 0.01$, *** $p \leq 0.001$, **** $p \leq 0.0001$.

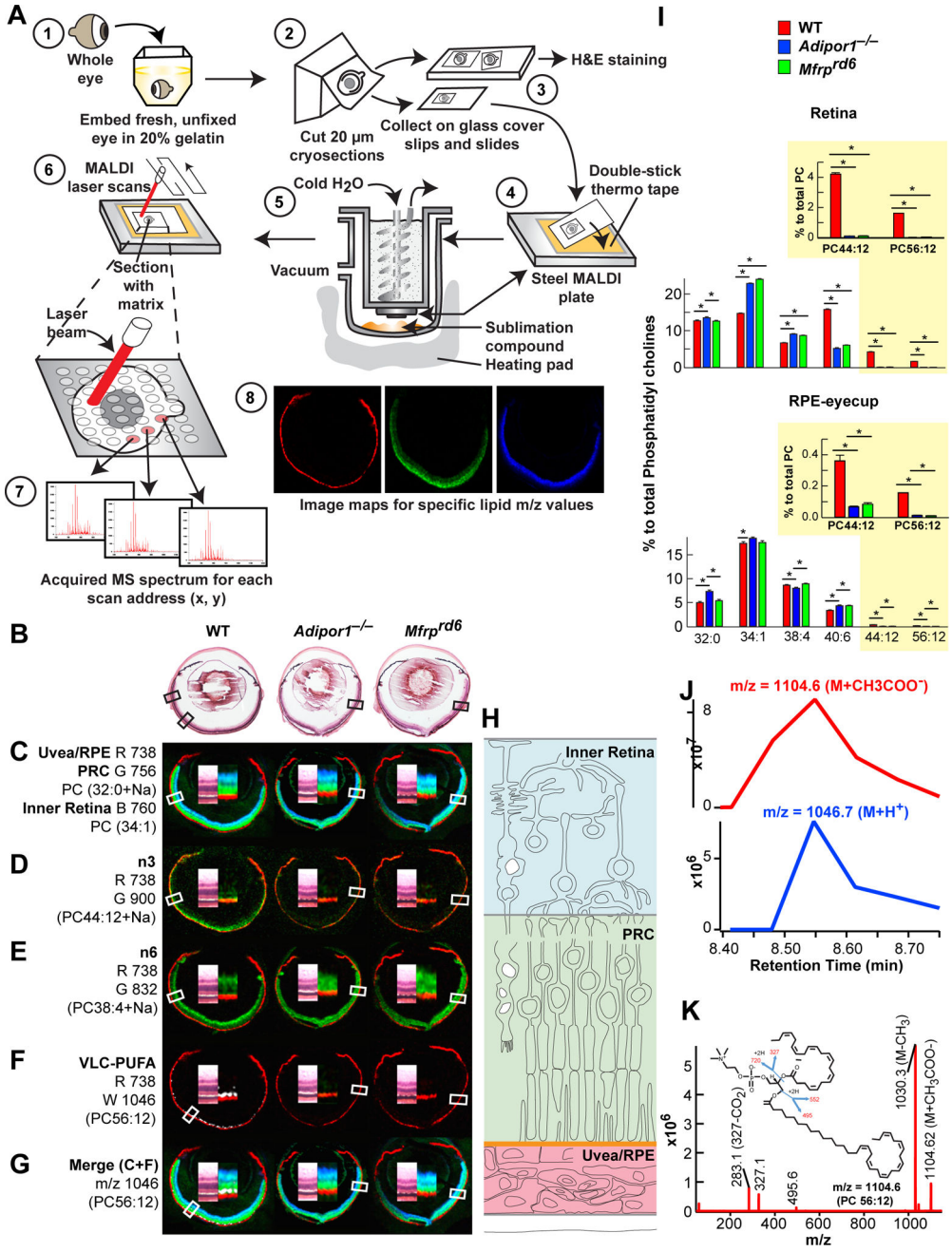

Fig. 2.

MALDI IMS reveals loss of PC containing 22:6 and VLC-PUFAs in the outer nuclear layer of *Mfrp*^{rd6} and *Adipor1*$^{-/-}$ retinas. **(A)** Whole eyes embedded in gelatin (1), frozen, cryosectioned, 20 µm (2), collected on alternating glass slides (for H&E) and coverslips (for MALDI) (3). Coverslips attached to MALDI plates (4) placed within sublimation chamber (55), matrix (2,5-dihydroxybenzoic acid, DHB) applied for positive ion mode analysis (5) MALDI Synapt G2-Si MS. Sections rastered by laser, 355 nm, 2000 Hz (6). Scanning control (30 µm, horizontal and vertical movement) and analysis. Image spot consisted of a collection of one second of data acquisition (7). Image processing (8). **(B)** H&E sections of

adjacent MALDI section for WT, *Adipor1*$^{-/-}$, and the *Mfrp*^{rd6} mice. **(C)** Lipid markers for uvea/RPE (m/z 738, red, R), PRC (m/z 756, green, G), and inner retina (m/z 760, blue, B). **(D)** n-3 containing PC(22:6/22:6), m/z 900 (green) is present in WT but absent in *Adipor1*$^{-/-}$ and *Mfrp*^{rd6} retinas. **(E)** n-6-containing phospholipids compensate D. Here, PC(18:0/20:4 n-6, m/z 832, green) is reduced in WT PRC, but still abundant within the inner retina while present within PRC of *Adipor1*$^{-/-}$ and *Mfrp*^{rd6}. **(F)** 22:6 is elongated to produce VLC-PUFAs. WT retina contains 34:6 within PC(34:6/22:6); 34:6 is indicated by the white label, while the *Adipor1*$^{-/-}$ and the *Mfrp*^{rd6} mice show no 34:6. **(G)** The merge of C and F illustrates the location of 34:6 just inside the uvea/RPE marker (red) at the outer region of PRC (green) in WT, but no label within mutant retinas (absence of 22:6). **(H)** Diagram on retinal location of C color markers. Double inset within each retina image is an enlargement of MALDI label and the corresponding area from H&E in B, indicated by boxes. N=3 for each condition. **(I)** LC-MS/MS quantitative PC molecular species distributions in bar graphs for retina (top) and RPE (bottom). 22:6-containing PCs, which are abundant in PRC outer segments, are reduced in *Adipor1*$^{-/-}$ and *Mfrp*^{rd6} retinas and RPE, especially PC 44:12 and PC 56:12 (yellow insets). Student's t-test (* $p<0.05$). **(J)** Retention time of negative ion mode of PC 56:12 (M+CH3COO) at m/z=1104.6 (top) matches with positive ion mode (M +H+) at m/z=1047.7, confirming that m/z=1046.7 measured in MALDI is from PC 56:12 (M +H+). **(K)** Full fragmentation spectrum of PC 56:12 (M+CH3COO-) measured in negative mode shows composition of PC 56:12 (34:6/22:6).

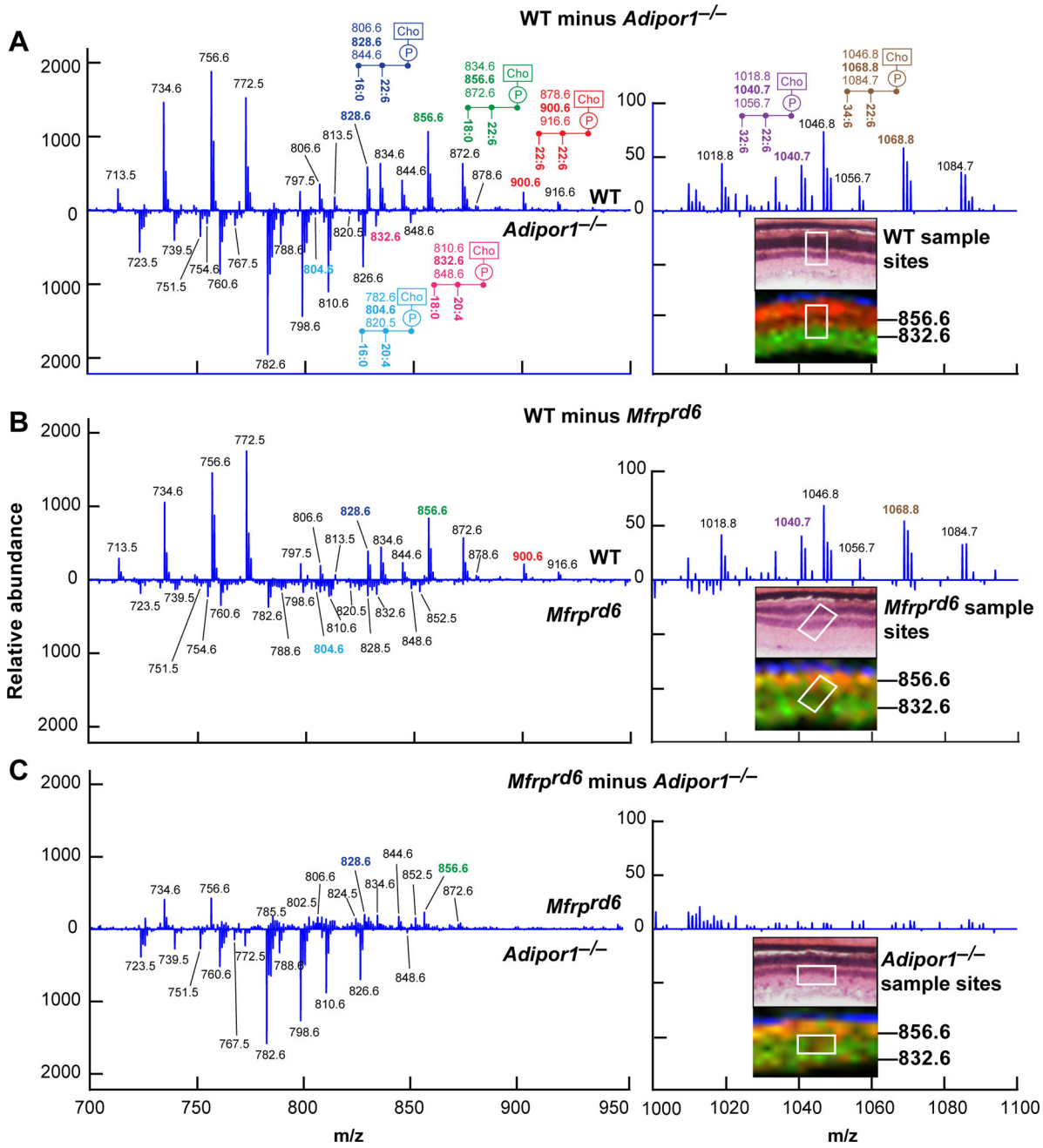

Fig. 3.

Differential MALDI spectra reveal compensatory PCs generated in *Adipor1*$^{-/-}$ and the *Mfrp*^{rd6} retina. Difference spectra show relative abundances detected by MALDI IMS. **(A)** Molecules more abundant in WT retina vs *Adipor1*$^{-/-}$ retina are presented in the upper part of the graph, while molecules more abundant in the *Adipor1*$^{-/-}$ retina are displayed at the bottom. 22:6- and/or VLC-PUFA-containing PCs are much more abundant in WT while 20:4-containing PCs are increased in the mutant retina. The regions from which the spectra are extracted are shown in the insert Fig. 5H,E (top) and MALDI (bottom), showing PC40:6 (m/z = 856.6, red) and PC38:4 (m/z = 832.6, green). The identification of the mass numbers

are shown in Supplemental Table 3. **(B)** The difference spectra of *Mfrp*^{rd6} to WT. **(C)** The difference spectra of *Adipor1*$^{-/-}$ to *Mfrp*^{rd6}. Inset images show that in both mutants, the PRC layers contain both PCs 40:6 and 38:4 (yellow) while WT has clear separation of the two PCs species between PRC layer and inner retina layer.

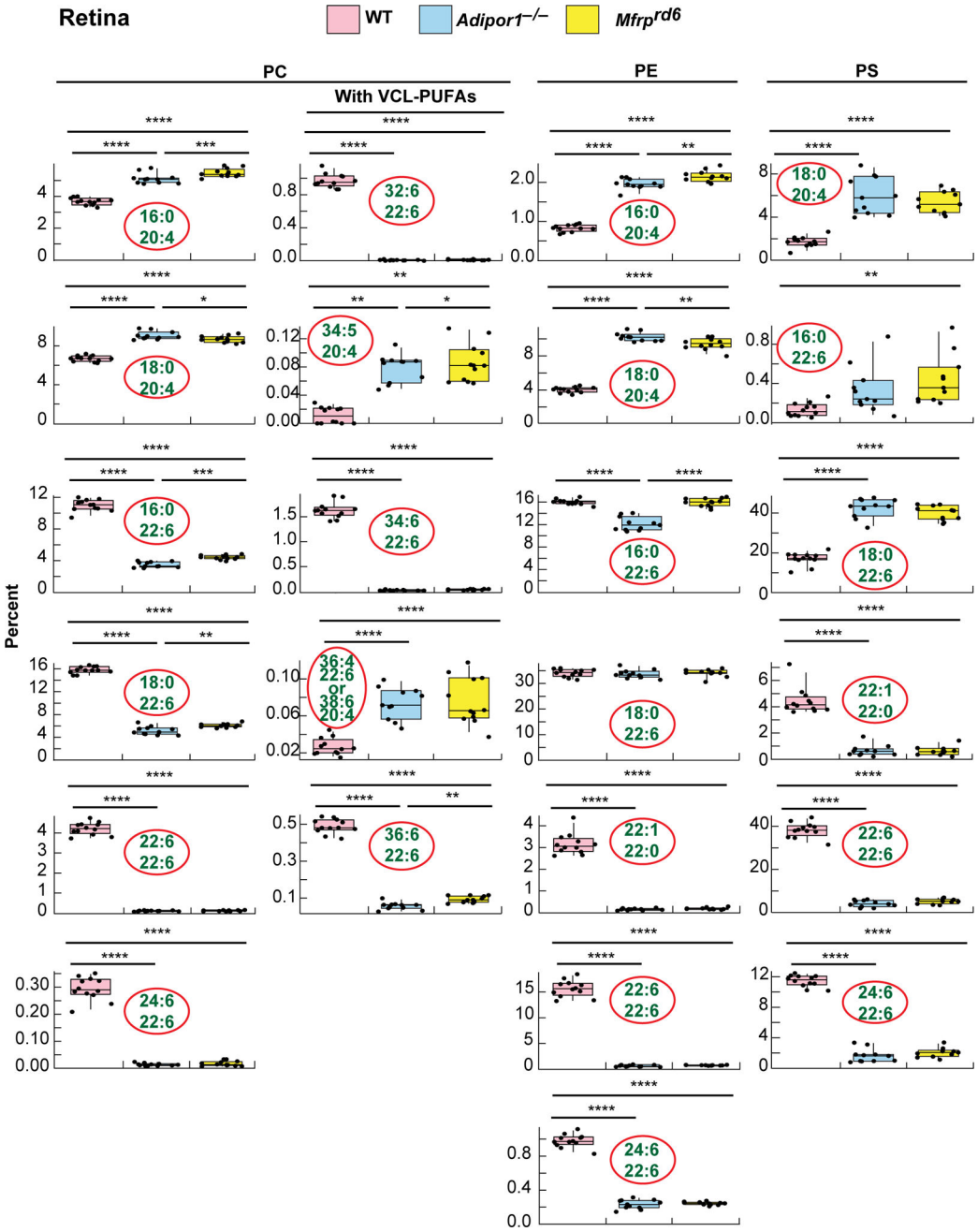

Fig. 4.

Selected phospholipid molecular species of WT, *Adipor1*$^{-/-}$, and *Mfrp*^{rd6} mouse retinas. 22:6- or 20:4-containing PC, PE and PS (except for PE(22:1/22:0) and PS(22:1/22:0)) are shown in the box plots. 20:4-containing PC, PE and PS are abundant in the mutant retinas. In both mutants, there is a great reduction of all the phospholipids containing two 22:6 molecules (PC, PE or PS(22:6/22:6)) and PCs composed of 22:6 and VLC-PUFAs (PC(22:6/32:6), PC(22:6/34:6), and PC(22:6/36:6)). On the other hand, single 22:6-containing PEs, such as PE(18:0/22:6), do not show differences among the groups, however, PE(22:6/24:6) shows greatly reduced amounts in both mutant retinas compared to WT.

Interestingly, non-22:6 or −20:4 containing PE(20:0/22:1), also shows great reduction in the mutants. For PS species, single 22:6-containing molecular species show higher abundances in the mutants while PS(22:6/24:6) and PS(22:0/22:1) show significant reduction in mutants.

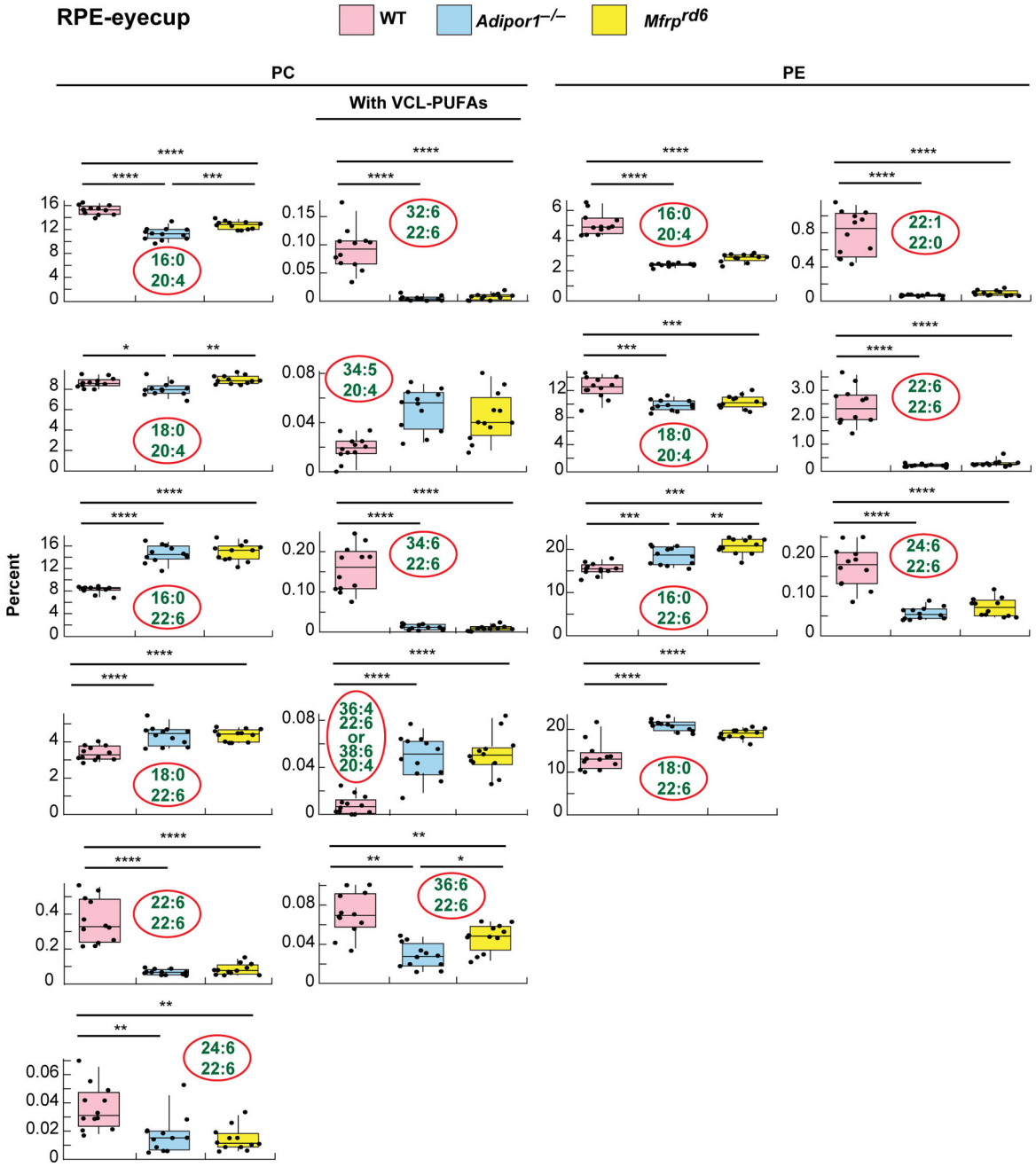

Fig. 5.

Box-plots of selected 22:6- or 20:4-containing PCs and PEs of WT, *Adipor1*$^{-/-}$, and *Mfrp*^{rd6} mouse RPE-eyecups. Most of the single 22:6-containing PC species in the RPE-eyecups show higher abundance in the mutants, unlike in the retinas. PC(22:6/22:6) or PC(22:6 combined with a VLC-PUFA) show great reduction in the mutants. 20:4-containing PE is reduced in the mutants, which is also an opposite observation from the retinas. Single 22:6-containing PEs are also increased in mutants, but PE (22:6/22:6) shows a great reduction in mutants, similar to the retina. Non-22:6 or 20:4 containing PE(20:0/22:1), also show great reduction in the mutants.

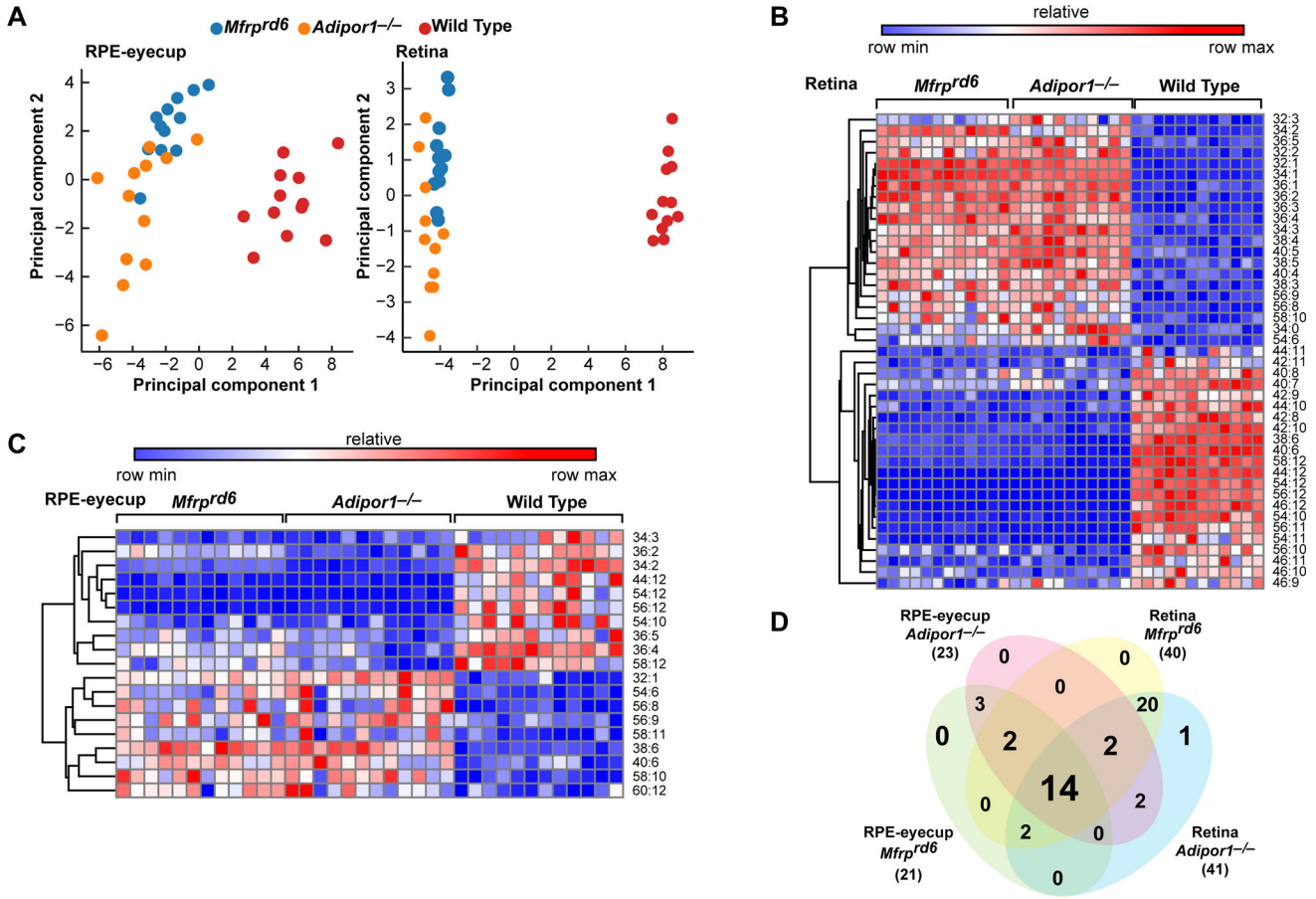

Fig. 6.

PCs containing VLC-PUFAs in *Adipor1*$^{-/-}$ and *Mfrp*^{rd6} eyes are greatly reduced. **(A)** Principal Component Analysis of targeted PCs illustrates tissue specific lipid profiles in mutants and WT mice (n=12). **(B)(C)** Hierarchical clustering of significantly differentially occurring PC species (Anova1-way) in *Adipor1*$^{-/-}$ and *Mfrp*^{rd6} retinas and RPE-eyecups compared to WT ($p \leq 0.05$, absolute value fold change ≥ 1.5) suggests compensatory PC dynamics. **(D)** Venn Diagram illustrates overlap of differentially occurring PCs across strains and tissues.

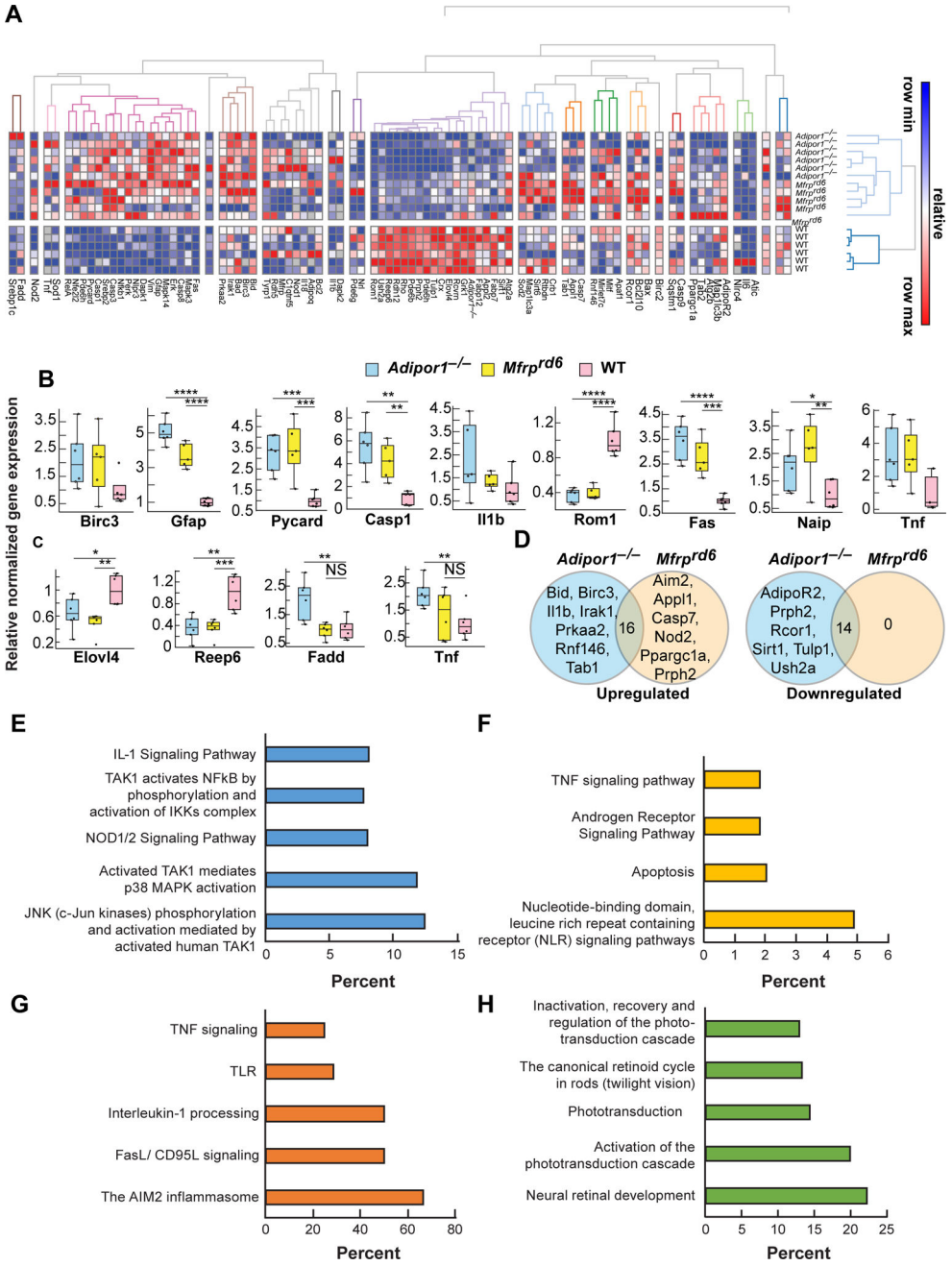

Fig. 7.

The expression of inflammatory markers is increased and visual system markers decreased in *Adipor1*$^{-/-}$ and *Mfrp*^{rd6}. **(A)** Heat map illustrating the hierarchical clustering of 88 target genes for the retinas of *Adipor1*$^{-/-}$ (n=6), *Mfrp*^{rd6} (n=5) and WT mice (n=6). Color key represents row scaling of normalized fold-change (FC) expression values from RT-qPCR. **(B)** Box-plots representation of selected genes for the retinas with their FC below −2 or above +2, relative to the WT. Boxes denote median values with upper and lower quartiles, and whiskers, minimum and maximum outliers. **(C)** Box-plots representation of selected genes for the RPE-eyecup samples with their FC below −2 or above +2, relative to WT. **(D)**

Venn diagrams of differentially expressed genes within *Adipor1*$^{-/-}$ and *Mfrp*^{rd6} datasets that are upregulated or downregulated in a statistically significant manner in the retina compared to the WT. The number in the intersection represents the differentially expressed genes that are common between the two datasets (Supplemental Table 1). Top pathways resulting from the upregulation of genes in *Adipor1*$^{-/-}$ retina **(E)** or *Mfrp*^{rd6} retina **(F)** compared to the WT, or common upregulated **(G)** or downregulated **(H)** genes in both mutant retinas. Student's t-test was used. * $p \leq 0.05$, ** $p \leq 0.01$, *** $p \leq 0.001$, **** $p \leq 0.0001$, NS=not significant. Error bars represent standard deviation. When there was no statistical difference in the mutant datasets compared to the WT, statistic bars were not added.